Received: 3 May 2021 | Revised: 6 January 2022 | Accepted: 7 January 2022

DOI: 10.1002/mp.15484

RESEARCH ARTICLE

MEDICAL PHYSICS

Vibration-controlled transient elastography for noninvasive evaluation of liver steatosis

Arthur Pearson[1,2] | **Paul-Armand Dujardin**[2] | **Louis d'Alteroche**[3] | **Frédéric Patat**[1,2,4] | **Béatrice Scotto**[1] | **Fanny Dujardin**[5] | **Cécile Bastard**[6] | **Véronique Miette**[6] | **Laurent Sandrin**[6] | **Jean-Pierre Remenieras**[4]

[1] Service de radiologie, CHRU de Tours, Tours, France

[2] CIC 1415, CHU de Tours, Inserm, Tours, France

[3] Service d'hépatologie, CHRU de Tours, Tours, France

[4] UMR 1253, iBrain, Université de Tours, Inserm, Tours, France

[5] Service d'anatomie et cytologie pathologiques, CHRU de Tours, Tours, France

[6] Echosens, Paris, France

Correspondence
Arthur Pearson, Radiology Department, Service de Radiologie, CHRU Bretonneau, 2 Boulevard Tonnellé, 37000 Tours, France.
Email: dr.arthur.pearson@gmail.com
Jean-Pierre Remenieras, Laboratoire Inserm 1253 imaging and Brain (iBrain), Université de Tours, 10 Bd Tonnellé, 37032 Tours
Email: jean-pierre.remenieras@univ-tours.fr

Funding information
CHRU de Tours; Echosens, Paris; Université de Tours

Abstract

Background: Nonalcoholic fatty liver disease (NAFLD) refers to a large spectrum of liver disorders and is the most common cause of metabolic liver disease. The current gold standard for diagnosing NAFLD is liver biopsy, which can lead to severe complications.

Purpose: Among the noninvasive diagnostic options, we chose to use a FibroScan and developed an algorithm applying the Voigt rheological model to assess the viscoelastic properties of the liver and evaluate its performance for the diagnosis of steatosis.

Methods: Twenty-two healthy volunteers and 20 patients with steatosis were included. For each subject, we used a modified FibroScan, whose data had been processed by our algorithm to separate the two viscoelastic components, stiffness μ, and viscosity η. The liver elasticity μFibroscan measured by the FibroScan was also recorded. Mann–Whitney tests and receiver operating characteristics (ROCs) curve analyses were performed to compare the parameters between the two groups, and Pearson's correlation coefficients were used to assess the correlations between the parameters.

Results: We found a good correlation between η and μFibroscan ($r = 0.75$), and poor correlations between μ and both η and μFibroscan ($r = 0.33$ and $r = 0.03$, respectively). We also showed that η and μFibroscan were higher in patients with steatosis compared to healthy volunteers, with area under the ROCs (AUROC) curve at 0.814 and 0.891, respectively. Conversely, μ was not different between the two groups (AUROC = 0.557).

Conclusions: Our novel method successfully separated the two viscoelastic properties of the liver, of which the parameter η is a sensitive indicator for steatosis.

KEYWORDS
elastography, fatty liver disease, NAFLD, shear elastic modulus, shear viscosity, shear wave, steatosis, VCTE

1 | INTRODUCTION

Nonalcoholic fatty liver disease (NAFLD) refers to a wide spectrum of liver disorders, ranging from benign isolated steatosis (NAFL) to Nonalcoholic Steatohepatitis (NASH), the latter ultimately evolving into cirrhosis and potential hepatocellular carcinoma.[1] It is the most common cause of metabolic liver disease, and its prevalence in the adult population is estimated at 25% worldwide, 80%–90% for obese adults, and

42.6%–69.5% for patients with type 2 diabetes.[2–4] NAFLD is currently a major public health concern, due to its increased risk of overall mortality, its liver-related morbidity and mortality, as well as an increased risk of type 2 diabetes, cardiovascular disease, and chronic kidney disease.[4–7]

The diagnostic gold standard for NAFLD is liver biopsy, which can distinguish simple steatosis (>5% of fat droplets within hepatocytes, usually estimated semi-quantitatively), from NASH and its characteristic inflammatory lesions, with or without fibrosis.[8,9] Its drawbacks are potentially severe complications (such as bleeding, or more rarely infection), sampling variability (small sample size, approximately 1/50 000th of the liver) and inter-observer variability.[10,11]

To overcome these limitations, noninvasive diagnosis of steatosis is routinely made by medical imaging; either prescribed due to symptoms or signs of liver disease, or incidentally discovered on thoracic and abdominal imaging prescribed for other reasons.[5] Most commonly, the diagnosis is made on morphological (B-mode) liver ultrasound (US), due to its wide availability, simplicity, low cost, and additional diagnostic yield.[12] But morphological US imaging has a moderate interobserver reproducibility and has limited sensitivity for mild steatosis (<30%).[13] Computed tomography can reliably diagnose hepatic steatosis. However, this technique presents two main problems: it is not sufficiently sensitive in the detection of mild steatosis (<30%) and exposes patients to radiation.[14,15] 1H Magnetic Resonance Spectroscopy (^{1}H-MRS) can identify spectral peaks that correspond to the protons in triglycerides and is considered one of the most sensitive imaging techniques for quantitative steatosis estimation but is not widely available and is technically challenging.[16] Magnetic resonance imaging (MRI) with calculation of Proton Density Fat Fraction (MRI-PDFF) is considered a better choice in routine practice compared to ^{1}H-MRS, as it is simpler to use and enables precise quantitative assessment of liver fat over the entire liver.[15] However, MRI-PDFF use is hampered by high costs and limited availability.[12,13,17] Although some advocate MRI as the new gold standard,[18,19] further validation of the latest techniques remains necessary.

In her recent PhD thesis, Imbault[20] developed a sound speed estimation method using an ultrafast scanner (Aixplorer, Supersonic Imagine, France). This method proposes a precise and robust in vivo sound speed assessment based on the spatial coherence analysis of a US beam at 3.5 MHz. The US speed is obtained from an optimal US beamforming in fatty liver. Imbault formulated the hypothesis that in hepatic steatosis, the liver is progressively transformed into a biphasic medium made of a mix of liver and fat cells. Using Wood's biphasic theoretical model, Imbault found a relation between the US fat fraction and the sound of speed measured within the liver. This US fat fraction was found to be highly correlated with MRI-PDFF in two 50-patient cohorts ($R^2 = 0.73$ and $R^2 = 0.76$, respectively).[21]

Another promising method is US attenuation measurement, which occurs during US compressional wave propagation in the liver. Compressional wave attenuation is due to viscous and scattering processes. The main difficulty with this approach is compensating US diffraction induced by beam spreading, to correctly separate attenuation due to viscous/scattering processes from attenuation due to beam diffraction. This attenuation measurement in the liver is performed with the controlled attenuation parameter (CAP),[22–26] using Fibroscan (Echosens, Paris, France), a US-based vibration-controlled transient elastography (VCTE) device that was initially created to assess liver fibrosis.[27–29] CAP can accurately diagnose steatosis but is limited for steatosis quantification. Although some authors have begun to create quantification cut-off values, a consensus has not yet been established.[12,15,26]

These techniques use compression waves in the megahertz range but it is also of interest to study the frequency dispersion of the shear wave speed in the 50–500 Hz range.[30,31] Nightingale et al. used shear wave dispersion analysis in the bandwidth 73–298 Hz and estimated the dispersion curve slope, which is related to the viscosity. They found a correlation between these parameters and fibrosis, but no correlation with steatosis.[32]

Prior to the study of Nightingale et al., we developed our own inverse problem to estimate the viscoelasticity of the liver using a modified Fibroscan sequence. Our main objective was to validate our algorithm as a tool for detection and quantification of liver steatosis, comparing healthy subjects and patients with steatosis confirmed by liver biopsy. Our secondary objectives were to describe the measured parameters in both groups, to evaluate the impact of age on our measurements and to study the correlation between our measurements and an MRI fat estimation.

2 | THEORY

2.1 | Analytical expression of the shear wave generated by the Fibroscan

The active part of the Fibroscan is a circular vibrator of radius $R = 4.5$ mm which is applied perpendicularly to the skin surface. This extended source, located in the plane $z = 0$, works in a piston mode and generates a uniform force $\boldsymbol{a} = (0, 0, a)$ over its surface S. The temporal evolution of the force $f(t)$ is a one period of sinusoid centered at 50 Hz. The induced tissue displacement $u_z(z, t)$ on the symmetry axis z is a convolution between

$f(t)$ and the impulse response $\mathcal{G}_{zz}(z,t)$ of the piston

$$u_z(z,t) = f(t) * \mathcal{G}_{zz}(z,t) = f(t) * \frac{aR^2}{\rho_0 \sqrt[3]{z^2+R^2}} \int_0^{\frac{\sqrt{z^2+R^2}}{c_{s_0}}} \tau\delta(t-\tau)\,d\tau, \quad (1)$$

where ρ_0 is the mass density of the medium, and c_{s_0} is the shear wave speed in a purely elastic medium.[33] Due to the Dirac function presence in $\mathcal{G}_{zz}(z,t)$, the integral term is a temporal ramp t, which evolves between the two times[33] $t_1 = 0$ to $t_2 = \frac{\sqrt{z^2+R^2}}{c_{s_0}}$. Initially t_1 is zero due to the high speed of the compressional waves (1500 m/s), which implies a virtually instantaneous propagation time for these waves compared to the timescale of the shear wave c_{s_0} (which propagates on the m/s order). Then $t_2 = \frac{\sqrt{z^2+R^2}}{c_{s_0}}$ and corresponds to the propagation time from the furthest source point, which contributes to the radiation on axis. This integral term is similar to the near field term of the elastodynamic Green function for a point force at the origin in an infinite medium with the axial distance z replaced by $\sqrt{z^2+R^2}$ corresponding to the distance from the edge of the circular piston to the observation point located on z axis.[34] For the frequency analysis of the radiated wave, we need to compute the Fourier transform of Equation (1), which is proportional to $F(\omega) \int_0^{\frac{\sqrt{z^2+R^2}}{c_{s_0}}} te^{-i\omega t}dt$. The proportionality term is $\frac{aR^2}{\rho_0\sqrt[3]{z^2+R^2}}$, which is situated in front of the integral. The first term $F(\omega)$ is the Fourier transform of the Fibroscan temporal excitation $f(t)$. The second term is estimated using an integration by parts that gives

$$\int_0^{\frac{\sqrt{z^2+R^2}}{c_{s_0}}} te^{-i\omega t}dt = \frac{1}{\omega^2}\left(1 + i\omega\frac{\sqrt{z^2+R^2}}{c_{s_0}} - e^{i\omega\frac{\sqrt{z^2+R^2}}{c_{s_0}}}\right)e^{-i\omega\frac{\sqrt{z^2+R^2}}{c_{s_0}}}. \quad (2)$$

For a given angular frequency ω, this diffraction term only depends on the distance $\sqrt{z^2+R^2}$ and for large z, Equation (2) may be written $\frac{iz}{\omega c_{s_0}}e^{-i\frac{\omega}{c_{s_0}}z}$. Thus the tissue displacement $u_z(z,\omega)$ is expressed as

$$u_z(z,\omega) = \frac{iaR^2}{\rho_0 z^2}\frac{F(\omega)}{\omega c_{s_0}}e^{-i\frac{\omega}{c_{s_0}}z}. \quad (3)$$

In the experimental part of this study, we use a tissue Doppler algorithm to estimate the axial particle velocity, then for inverse problem solving, we need to determine the analytical expression of the tissue particle velocity $v_z(z,f)$. This is simply obtained by multiplying the tissue displacement $u_z(z,f)$ by $-i\omega$. Finally, we obtain the required expression

$$v_z(z,f) = \frac{aR^2F(f)}{\rho_0 c_{s_0}}\frac{1}{z^2}e^{-ikz} \quad (4)$$

where $k = \frac{2\pi f}{c_{s_0}}$ is the shear wave number in an assumed purely elastic media.[34] The shear velocity can be expressed as $c_{s_0} = \sqrt{\frac{\mu}{\rho_0}}$ with μ the shear elastic modulus. In a purely elastic soft media, the wave speed c_{s_0} is independent of the frequency. In the human body, the soft tissues are mainly composed of water and thus are considered nearly incompressible; the Young modulus E is linked to μ by the relation $E = 3\mu$ as the first Lamé coefficient λ is much higher than μ. In Equation (4), the radiated wave amplitude $|v_z(z,f)|$ is inversely proportional to c_{s_0}, so the wave amplitude will be greater in a soft liver with a low μ than in a hard liver. We also note that the spatial decay is inversely proportional to the square of the distance z.

Using a rheological model, viscoelasticity can be introduced[35] by a complex elastic modulus $G(f) = G'(f) + iG''(f)$, which implies a complex wave number

$$k(f) = \frac{2\pi f}{c_s(f)} - i\alpha(f) \quad (5)$$

where $\alpha(f)$ is the frequency dependent attenuation coefficient. The phase velocity is expressed as $c_s(f) = 2\pi f/R[k(f)]$ and, compared to c_{s_0}, is modified by the shear viscosity term $G''(f)$. Finally, the particle velocity of the attenuated wave generated by the Fibroscan in the viscoelastic liver for large z is expressed as

$$v_z(z,f) = \frac{aR^2E(f)}{\rho_0 c_s(f)}\frac{e^{-\alpha(f)z}}{z^2}e^{-i\frac{2\pi f}{c_s(f)}z}. \quad (6)$$

It is interesting to note that in a viscoelastic medium, both the shear velocity $c_s(f)$ and the attenuation coefficient $\alpha(f)$ depend on the frequency f. These acoustic parameters are linked to the tissue's biomechanical parameters through a rheological model.

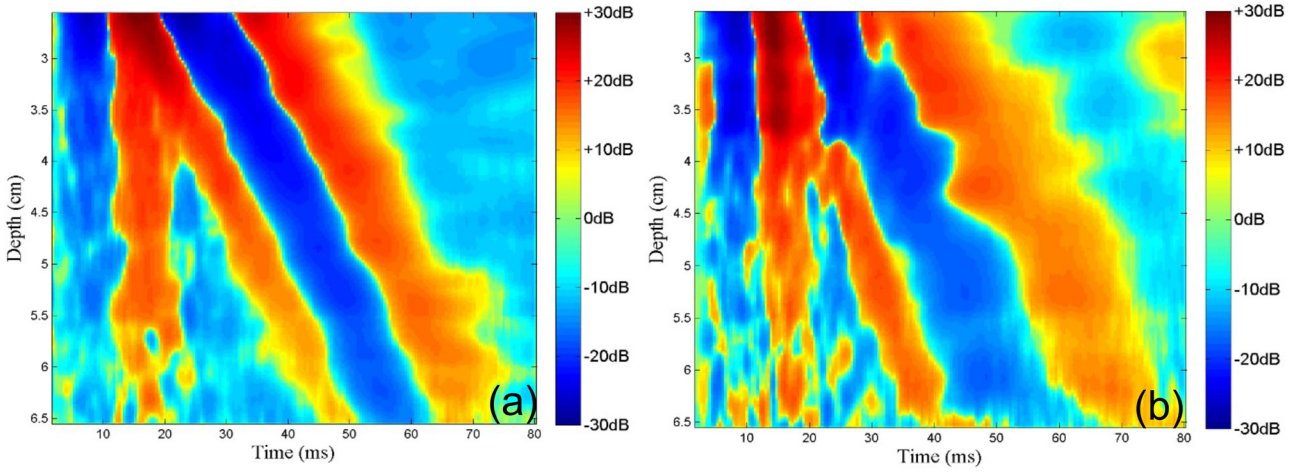

FIGURE 1 Example of in vivo spatio-temporal wave particle velocity v_z (z,t) in the liver for a healthy volunteer (a) and a patient (b). The transient temporal excitation f(t) is the same for these two elastograms

2.2 | Estimation of the group velocity

The classical measurement of the Fibroscan estimates the group velocity of the wave packet created by the vibrator situated at the surface of the skin above the liver. This group velocity is estimated from the slope of the spatio-temporal elastogram[27] (Figure 1).

The frequency bandwidth is 25–85 Hz, and the maximum amplitude of the shear wave is situated at around 50 Hz. This group velocity c_{Fibro} corresponds mainly to the phase velocity where the wave amplitude is the greatest, that is, at 50 Hz. From this velocity c_{Fibro} and assuming a purely elastic medium (which is not valid in the case of viscoelasticity), the shear elastic modulus μ_{Fibro} can be computed using the relation $\mu_{\text{Fibro}} = \rho_0\, c^2_{\text{Fibro}}$.

2.3 | Estimation of phase velocity dispersion $c_s(f)$

Muller et al.[31] extracted the phase velocity $c_s(f)$ from the phase $\Phi(z,f) = -Re[k(f)]z$ of $v_z(z,f)$ unwrapped along the z-axis for each frequency. The phase is fit along the distance z to retrieve the real part of the wave number $k(f)$ for each frequency. The number of points used for the linear fit is adjusted for each frequency because attenuation limits the propagation distance of the high-frequency components of the shear wave. The automatic choice of this number of fitting points is based on rejecting the unaligned points at high frequency (large values of z), which would dramatically decrease the quality of the wave number estimation. Nightingale et al.[32] used space and time 2D Fourier transform $v_z(f_z,f)$ of the elastogram $v_z(z,t)$ and estimated for each frequency f the position $f_{z_{\text{Max}}} = 1/\lambda$ corresponding to the maximum of the spatial spectrum. The velocity is obtained for each frequency with the relation $c_s(f) = f/f_{z_{\text{Max}}}$.

Leclerc et al.[36] used Magnetic Resonance Elastography, with an identification method estimating the wavelength on MRI phase images for different frequencies in the direction of the shear wave propagation. For our method, we adapted this idea to 1D transient elastography. For each frequency, we normalized the in vivo axial particle velocity $v_z(z,f)$ by the axial particle velocity $v_z(z_0,f)$ obtained for the first acquired point at the distance z_0. The ratio $\mho(z,z_0,f)$, which is a complex number $A+iB$, follows the analytical relation given by Equation (7) with $\Delta z = z - z_0$

$$\mho(z,z_0,f) = \frac{v_z(z,f)}{v_z(z_0,f)} = \frac{e^{-\alpha(f)\Delta z}}{(z/z_0)^2}\, e^{-i\frac{\omega}{c_s(f)}\Delta z} = \frac{e^{-\alpha(f)\Delta z}}{(z/z_0)^2}\left(\cos\left(\frac{2\pi}{\lambda(f)}\Delta z\right) - i\sin\left(\frac{2\pi}{\lambda(f)}\Delta z\right)\right) \tag{7}$$

This normalization enables the real part $R[\mho(z,z_0,f)]$ of $\mho(z,z_0,f)$ to start at the unit value and the imaginary part $I[\mho(z,z_0,f)]$ to start at the value zero.

One can observe in Figure 2a the $1/f$ evolution of the 2D wave field pattern, which is in agreement with the decrease of the wavelength with frequency $\lambda(f) = c_s(f)/f$. Using a nonlinear least squares solver, we conjointly fit the real and imaginary parts of the in vivo data as a function of z with the theoretical model $\mho(z,z_0,f)$ given by Equation (7). The two variables to be identified are the attenuation $\alpha(f)$ and the wavelength $\lambda(f)$ for a particular selected frequency f. In Figure 2b, we clearly see the quadrature between the real part $\cos(\frac{2\pi}{\lambda(f)}\Delta z)$ and the imaginary

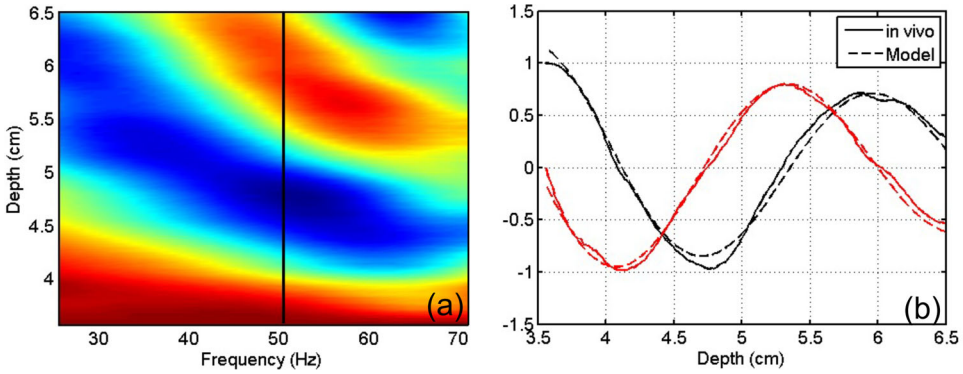

FIGURE 2 (a) Real part $\Re[\mathfrak{V}(z, z_0, f)]$ of the experimental data $\mathfrak{V}(z, z_0, f)$ in the bandwidth (25 Hz–70 Hz) as a function of the axial distance z for a volunteer. The phases at the origin are zero. When frequency increases, the wavelength λ decreases and the number of waves in the fixed analysis distance (i.e., [3.5 cm–6.5 cm]) increases. (b) Real part $\Re[\mathfrak{V}(z, z_0, f = 50Hz)]$ (black continuous line) and the imaginary part $\Im[\mathfrak{V}(z, z_0, f = 50Hz)]$ (red continuous line) of the experimental data $\mathfrak{V}(z, z_0, f)$ overlayed with the theoretical propagation model (dashed lines) of (7). These data are computed at 50 Hz at the vertical line position of Figure 2a

part $-\sin(\frac{2\pi}{\lambda(f)}\Delta z)$ of $\mathfrak{V}(z, z_0, f)$, and the decay of the wave magnitude as a function of the propagation distance z. The shear velocity $c_s(f)$ is then deduced from the wavelength $\lambda(f)$ obtained for each frequency by the relation $c_s(f) = \lambda(f) \cdot f$. This method is well adapted for in vivo data because the algorithm is mainly influenced by $\mathfrak{V}(z, z_0, f)$ for a distance z near to z_0, where the signal-to-noise ratio is high. The quadrature between the real and imaginary parts of $\mathfrak{V}(z, z_0, f)$ is also useful for the identification algorithm, because background noise is inconsistent with this property. From the curve shown in Figure 2b, we obtained $\lambda\ (f = 50\ \text{Hz}) = 2.5$ cm with the inverse problem solving, namely $c_{s_{\text{exp}}}\ (f = 50\ \text{Hz}) = 1.25\text{m/s}$. At the end of this multi-frequency procedure, we experimentally obtained the dispersion curve $c_{s_{\text{exp}}}(f)$. With Equation (7), it is theoretically possible to estimate both $c_s(f)$ and $\alpha(f)$ from experimental data. The attenuation is estimated from the $\frac{e^{-\alpha(f)z}}{z^2}$ part of Equation (7), namely the additional deviation from the predictive diffraction proportional to $1/z^2$. In practice, it is difficult to accurately estimate this attenuation coefficient in vivo in the liver due to the highly variable amplitude evolution of the shear wave during its propagation. For example, if the liver is not purely homogeneous in the selected region of interest (ROI) and if the elasticity slowly decreases with z, the shear velocity will then decrease, and the amplitude of the wave will increase with z since c_s is at the denominator of Equation (6). In this case, it is possible to have an amplitude decrease of the wave inferior to diffraction prediction, which is interpreted by the algorithm as a negative viscous attenuation. The positions of the vibrator between the ribs can sometimes also influence the decay of the shear wave with z. For these reasons, we only focused on the dispersion analysis of the shear velocity $c_s(f)$ with frequency.

2.4 | Voigt rheological model

We chose the simple Voigt model with the viscoelastic parameters (μ, η) where μ is the shear modulus, and η is the shear viscosity. We chose this rheological model because there are few parameters to estimate, and with this model, the shear velocity $c_s(f)$ dispersion curve at low frequency is simply adjusted by the ratio $\eta\omega/\mu$, which enabled us to estimate η considering the value of the shear elastic modulus μ. The relation between $c_s(f)$ and (μ, η) is given by Catheline et al.[37]

$$c_s\ (f) = \sqrt{\frac{2\left(\mu^2 + \omega^2\eta^2\right)}{\rho_0\left(\mu + \sqrt{\mu^2 + \omega^2\eta^2}\right)}} \tag{8}$$

with $\omega = 2\pi f$. The viscoelastic parameters μ and η can be easily obtained by fitting the model Equation (8) to the dispersion curve $c_{s_{\text{exp}}}(f)$ obtained experimentally. In the liver, we typically obtain $c_s(f = 0) \approx 1m/s$ and $\eta \approx 1\ Pa \cdot s$, giving a shear parameter $\mu = \rho_0\ c_s^2\ (0) = 1$ kPa. With these viscoelastic parameters of the liver, $\omega^2\eta^2/\mu^2 = 0.1$ at 50 Hz. At this frequency, the shear wave is not evanescent, and the viscous effect $\omega\eta$ is small compared to elasticity μ. Using the Taylor series expansion of Equation (8) for $\omega^2\eta^2/\mu^2 \to 0$, Equation (8) can be simplified

$$c_{s_{\omega^2\eta^2/\mu^2 \to 0}}\ (f) = c_{s_0}\left(1 + \frac{3}{8}\frac{\omega^2\eta^2}{\mu^2}\right) \tag{9}$$

where $c_{s_0} = c_{s_{\omega^2\eta^2/\mu^2 \to 0}}\ (0) = \sqrt{\mu/\rho_0}$ is the shear wave velocity in a linear purely elastic medium. Equation (9) shows that the viscous effect modifies the shear phase velocity in function of the frequency and the relative velocity variation $(c_{s_{\omega^2\eta^2/\mu^2 \to 0}}(f) - c_{s_0})/c_{s_0}$ is simply

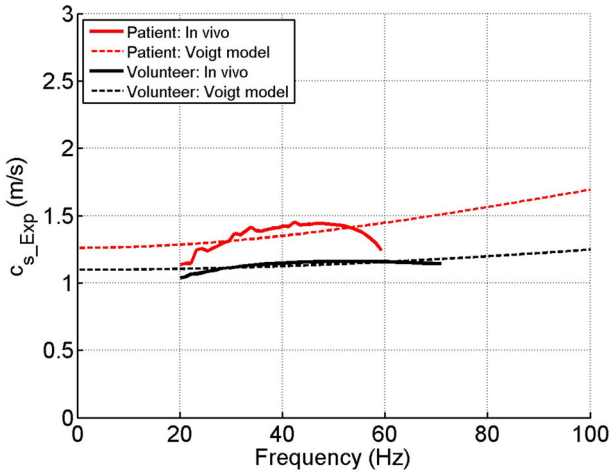

FIGURE 3 Shear wave dispersion curve between [20 Hz–70 Hz] for one volunteer and one patient overlayed with the theoretical Voigt model given by (9)

$\frac{3}{8}(\frac{\omega\eta}{\mu})^2$. In the Voigt model, the ratio between the imaginary part and the real part of the complex elastic modulus $G = \mu + i\eta\omega$ controls the dispersion curve. Thereby, for a constant value of viscosity η, the rate of slope change with frequency $\frac{\partial^2 c}{\partial f^2} = \frac{3\pi^2\eta^2}{\sqrt{\rho_0\mu^3}}$ will be smaller for a stiff liver (i.e., with high μ) than for a soft liver. Inversely, with an identical variability of the dispersion curve but simply positioned at a different position on the vertical axis (i.e., different $c_s\,(f = 0) = \frac{\mu}{\rho_0}$), the resulting viscosity η will be estimated lower by the algorithm for a soft liver than for a stiff liver. It is interesting to note that with Equation (9), the shear elasticity μ is estimated by the fitting algorithm from the origin position $c_s(f = 0)$ of the dispersion curve $c_s(f)$. The algorithm extrapolates this position because no measurement is obtained at zero frequency. The shear viscosity coefficient η is estimated to follow the frequency evolution of $c_{s_{\omega^2\eta^2/\mu^2\to 0}}(f)$ with μ fixed. Because the $c_s(f)$ curve is an increasing function with f, shear elasticity coefficient μ_{Voigt} corresponding to $c_s(0)$ is lower than μ_{Fibro} obtained from the group velocity situated mainly at 50 Hz. This group velocity is impacted by viscosity, which stiffens the liver. This remark is significant because, with a spectroscopy method, we can separate the effect of elasticity from the effect of viscosity if the organ follows the selected rheological model behavior.

In Figure 3, we assume a parabolic evolution of these curves even if the red dispersion curve seems to decrease for frequencies >50 Hz for the patient. For these acquisitions, the estimated viscoelastic parameters are $\mu = 1.21$ kPa, $\eta = 1.23$ Pa · s for the volunteer and $\mu = 1.59$ kPa, $\eta = 2.84$ Pa · s for the patient. We carried out 10 successive measurements and computed the median and interquartile range for the statistical analysis.

3 | MATERIALS AND METHODS

3.1 | Study design

This was an interventional, prospective, and single center study. Subjects were enrolled at the University Hospital of Tours between April 2013 and November 2015. The study was registered on ClinicalTrials.gov (NCT02575625) and was approved by a local ethics committee.

Our first step was to conduct a feasibility trial on a small number of healthy volunteers to develop our algorithm; its results, having no clinical implications, will not be detailed. Then we conducted a second trial comparing healthy volunteers to patients with steatosis without severe fibrosis.

3.2 | Patients

All healthy volunteers and patients gave their written informed consent. Neither pregnant women nor persons under guardianship were included.

Inclusion criteria for healthy volunteers were: age ranging from 18 to 65 years old, none or restricted alcohol consumption (≤ 20 g/day for women or ≤30 g/day for men), normal liver enzyme levels, and normal liver MRI. Inclusion criteria for patients were: steatosis assessed by a liver biopsy performed during the month before inclusion and scored using the steatosis, activitiy and fibrosis (SAF) score,[38,39] or during the preceding 2 years associated with an MRI confirming steatosis passed within the preceding month and persistently elevated liver enzymes.

Most of the exclusion criteria were common to both groups: presence of any liver tumor, ascites, infection caused by hepatitis virus or human immunodeficiency virus, exposure to poisonous chemicals (drugs, paints or solvents) during the last 4 weeks, known metabolic liver disease, autoimmune hepatitis, and contraindications to MRI. Specific exclusion criteria were the discovery of steatosis on imaging (US or MRI) during the trial for supposedly healthy volunteers, and the presence of severe fibrosis (fibrosis > F2 using the SAF score) on the patients' liver biopsy.

3.3 | Clinical, laboratory, and imaging data collection

Demographic and clinical information were recorded for each participant: age, sex, body-mass index, blood pressure, daily alcohol consumption, history of diseases. Fasting blood samples included dosage of liver enzymes, prothrombin time, cholesterol, triglycerides, glycemia, Hba1C, and insulinemia.

If liver MRI had not been performed before inclusion, then it was conducted after inclusion on an Ingenia 1.5T MRI system (Philips, The Netherlands). Axial triple echo gradient in-phase and out-phase sequences were performed on the liver to calculate fat fraction quantitatively on three different ROI within the liver with a dedicated program that included a correction for iron overload; the final result being the mean of the three ROI measurements.

Liver biopsy was performed before inclusion of the patients, as part of regular care.

3.4 | Modified Fibroscan measurements and posttreatment of data

Using an FS502 Fibroscan modified in partnership with Echosens (Paris, France), we performed our measurements on subjects positioned in dorsal decubitus, on an optimal measurement spot previously defined by a morphological US (good acoustic window and no blood vessel in the area).

Thirty excitations were done with a temporal vibration centered at 50 Hz, then the process was repeated centered at 75 Hz, for a total of 60 excitations per patient. The acquired data were then stored and transferred on a computer for processing. A MatLab (MathWorks Inc., Natick, MA, USA) algorithm was used to compute the values of elasticity (μVoigt) and viscosity (ηVoigt) of the Voigt model, as detailed in the Theory section. The Fibroscan default values (μFibroscan) were also extracted.

Only acquisitions validated by the classical Fibroscan algorithm were treated with the spectroscopy algorithm. Practically speaking, the computing of one acquisition (one excitation) required these steps: (1) The shear wave was selected on the elastogram for analysis via semi-automatic segmentation, and its Fourier transform was calculated. (2) The Fourier transform was then reviewed on a 2D graphic, and the optimal bandwidth was selected manually. (3) Our algorithm estimated μVoigt and ηVoigt, and μFibroscan was extracted from the data. (4) For each patient, the final measure was the median of the parameters μ and η calculated from the validated excitations.

3.5 | Statistical analysis

Patients were described using quartiles for quantitative variables, and numbers and percentages for qualitative variables.

First, measured parameters between patients with steatosis and healthy volunteers were compared using Mann–Whitney tests. Then, for each parameter, an receiver operating characteristic (ROC) curve was computed, and its area under the curve (AUROC) was calculated. The same analysis was performed by using the results of a logistic regression with steatosis diagnosis as response variable and μVoigt and ηVoigt as explanatory variables, at 50 Hz and 75 Hz.

For all subjects, the correlations between the measured Fibroscan parameters were evaluated using Pearson's correlation coefficients and their 95% confidence interval (CI).

A correlation was also evaluated between μFibroscan and the combination of the parameters μVoigt and ηVoigt. To do this, two logistic regressions were evaluated, both with steatosis diagnosis as response variable: the first was realized with μFibroscan as explanatory variable and the second with μVoigt and ηVoigt as the explanatory variables. Finally, a correlation between the results of these two logistic regressions was performed using Pearson's correlation coefficient.

For the evaluation of the impact of steatosis stage on measured parameters, we first calculated steatosis stage using macrovesicular steatosis (MS) on histologic evaluation: S0 for MS $<$ 5% ; S1 for 5% $\leq$ MS $\leq$ 33%, mild; S2 for 34 $\leq$ MS $\leq$ 66%, moderate; and S3 for MS $\geq$ 67%, marked.[38] Then, we joined some stages and evaluated two groups: S0S1 comprising S0 and S1 stages, and S2S3 comprising S2 and S3 stages. After that, the measured parameters between these two groups were compared using Mann–Whitney tests. Finally, the ROC curves were also computed and their corresponding AUROC and 95% CI calculated.

Correlations between MRI fat fraction and Fibroscan parameters were also evaluated, using Pearson's correlation coefficient.

For the evaluation of the impact of age on measured parameters, we first separated the data of our healthy volunteers into two groups; one with subjects $\leq$30 years old, and the other with subjects $\geq$40 years old. Then, the measured parameters of the two groups were compared using Mann–Whitney tests.

Statistical analyses were performed using MatLab release R2007b. A *p*-value of 0.05 was considered as significant.

4 | RESULTS

4.1 | Study population characteristics

A total of 72 participants were enrolled in the study: 48 healthy volunteers and 24 patients with steatosis. Nine participants were excluded: seven healthy volunteers (one discovery of a hepatic lesion, four had intercurrent elevation of liver enzymes, and two had steatosis on imaging) and two patients (one discovery of severe fibrosis and one withdrawn consent). Sixty-three participants finished the study, of which 11 had data that were not of sufficient quality for analysis (nine healthy volunteers and two patients).

TABLE 1 Healthy volunteers and patients' characteristics

	Healthy volunteers ($n = 22$)	Patients ($n = 20$)
Age (years)	29 (26–45)	55 (52–60)
Sex	Male: 5 (22.7%)	Male: 11 (55%)
	Female: 17 (77.3%)	Female: 9 (45%)
Weight (kg)	65 (56–72)	87 (74–91)
Height (cm)	162 (160–172)	171 (159–176)
Body mass index (kg/m^2)	23.7 (21.0–25.5)	29.2 (27.1–31.7)
Waist circumference (cm)	82 (75–88)	101 (96–108)
Steatosis stage*	S0: 22 (100%)	S1: 6 (30%)
		S2: 9 (45%)
		S3: 5 (25%)

Estimated by MRI fat fraction for healthy volunteers (all values were < 3%), measured on histological examinations for patients, using the SAF score.

Of the remaining 52 participants, 10 were healthy volunteers who participated in the feasibility trial, and 42 (22 healthy volunteers, 20 patients) in the main trial. The clinical data of the 42 participants in the main trial are available in Table 1.

Detailed pathological SAF score for each patient is available in supplementary material (Table S1)

4.2 | ηVoigt and other parameters for steatosis evaluation

ηVoigt was significantly higher for patients with liver steatosis (≥S1) compared with healthy volunteers (S0), both for the 50 Hz excitations (3.0 Pa·s [2.3–3.3] vs. 2.1 Pa·s [1.7–2.4]; $p < 0.001$) and for the 75 Hz excitations (2.3 Pa·s [1.9–2.8] vs. 1.8 Pa·s [1.7–2.1]; $p < 0.002$). μFibroscan also presented higher values for patients with steatosis (2575 Pa [2000–3117] vs. 1417 Pa [1183–1667]; $p < 0.001$) (Figure 4).

Combined ηVoigt + μVoigt was significantly higher for patients with liver steatosis compared with healthy volunteers at 50 Hz ($p < 0.001$) and 75 Hz ($p = 0.0028$).

On the other hand, μVoigt was not significantly different between the two groups, both for the 50 Hz excitations (999 [681–1396] vs. 1091 [992–1274]; $p = 0.54$) and for the 75 Hz excitations (1077 [793–1325] vs. 1064 [947–1226]; $p = 1$) (Figure 5).

4.3 | Diagnostic performance for steatosis of ηVoigt, μVoigt, and μFibroscan

Table 2 provides the characteristics of each Fibroscan parameter for the diagnosis of steatosis. Comparing healthy volunteers (S0) versus steatosis (≥ S1), our measures of ηVoigt had an AUROC of 0.814 (0.680–0.947) for the 50 Hz excitations and 0.784 [0.642–0.926] for the 75 Hz excitations. Conversely, μVoigt measures had an AUROC of 0.557 (0.381–0.733) for the 50 Hz excitations and 0.500 (0.323–0.677) for the 75 Hz excitations (Figure 6).

μFibroscan had an AUROC of 0.891 (0.787–0.995), while the combination of ηVoigt and μVoigt had an AUROC of 0.893 (0.790–0.996) for the 50 Hz excitations (Figure 7), and an AUROC of 0.770 (0.625–0.916) for the 75 Hz excitations (figure available in supplementary materials (Figure S1)).

Combining S0 and S1 stages on one side and S2 and S3 on the other, the AUROCs for the diagnosis of steatosis ≥S2 with the 50 Hz excitations were of 0.875 (0.748–1) for ηVoigt, 0.587 (0.399–0.774) for μVoigt and 0.901 (0.786–1) for μFibroscan (Figure 8). With the 75 Hz excitations, they were of 0.829 (0.684–0.974) for ηVoigt, 0.469 (0.284–0.655) for μVoigt, and 0.802 (0.649–0.956) for μFibroscan (figures in supplementary materials [Figure S2]).

4.4 | Correlations between ηVoigt, μVoigt, and μFibroscan

Correlations between each parameters were assessed; the coefficients are available in Table 3.

ηVoigt and μFibroscan were well correlated, for the 50 Hz excitations and the 75 Hz excitations ($r = 0.75$ [0.58–0.86], $p < 0.001$ and $r = 0.62$ [0.43–0.8], $p < 0.001$, respectively). On the other hand, μVoigt was not correlated with μFibroscan ($r = 0.03$ [−0.26–0.33], $p = 0.868$ for the 50 Hz excitations, and $r = 0.07$ [−0.24–0.36], $p = 0.679$ for the 75 Hz excitations), was weakly correlated to ηVoigt for the 50 Hz excitations ($r = 0.33$ [0.03–0.58] $p = 0.0317$), and was not correlated to ηVoigt for the 75 Hz excitations ($r = 0.13$ [−0.18–0.41] $p = 0.425$).

Logistic regression analyses found a good correlation comparing μFibroscan with the combination of ηVoigt and μVoigt ($r = 0.776$ [0.618–0.874] $p < 0.001$).

4.5 | Correlation between the Fibroscan parameters and MRI fat fraction

ηVoigt was moderately correlated with MRI fat fraction ($r = 0.49$ [0.21–0.69], $p = 0.0013$ and $r = 0.34$ [0.03–0.58], $p = 0.03$ for the 50 Hz and 75 Hz excitations, respectively), as was μFibroscan ($r = 0.54$ [0.28–0.73], $p < 0.001$). On the contrary, μVoigt was not correlated with MRI fat fraction ($r = 0.16$ [−0.15–0.45], $p = 0.3$ for the 50 Hz excitations and $r = 0.13$ [−0.19–0.42], $p = 0.43$ for the 75 Hz excitations).

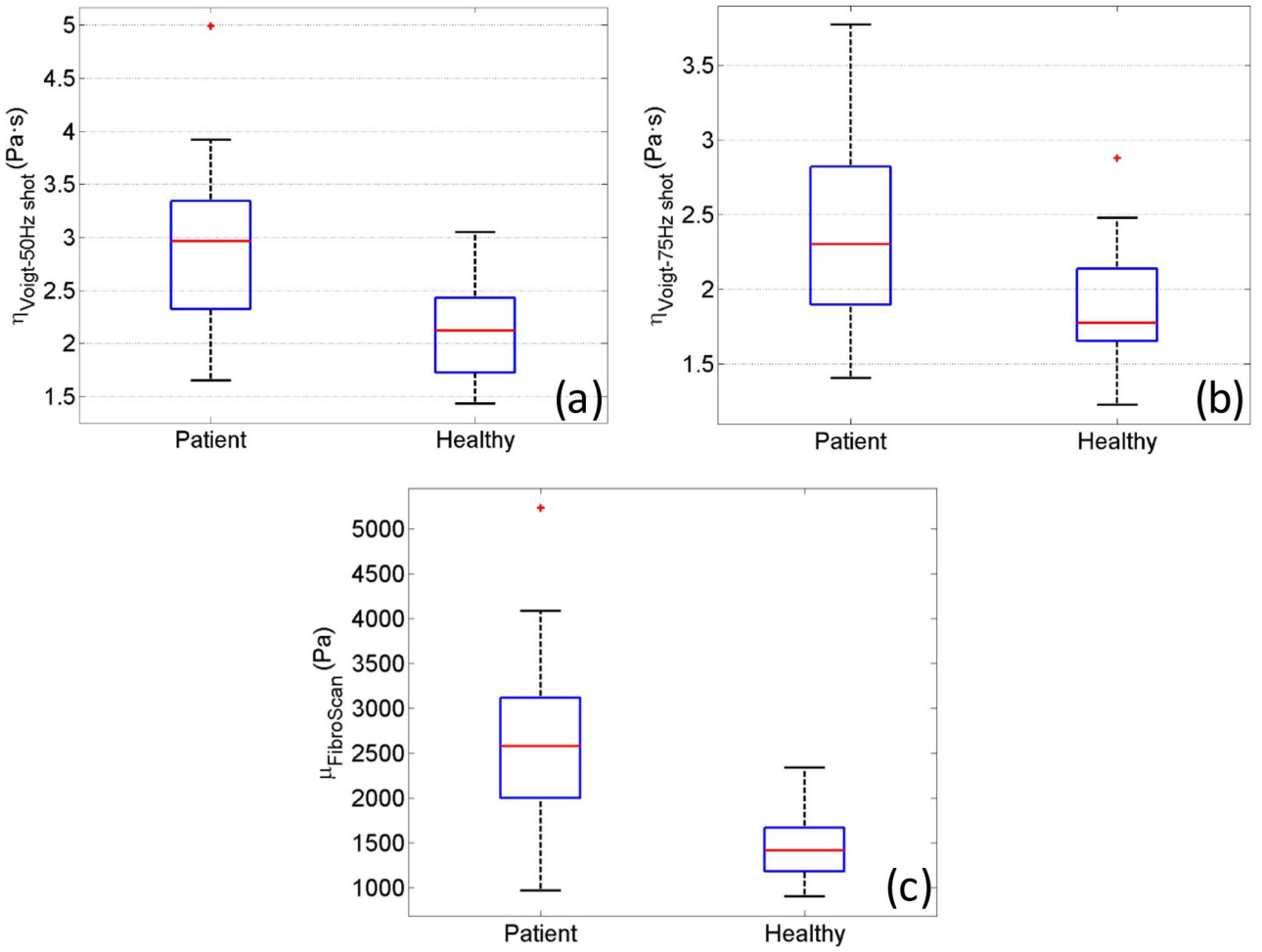

FIGURE 4 Boxplots of the parameters ηVoigt for the 50 Hz excitations (a), 75 Hz excitations (b) and μFibroscan (c)

FIGURE 5 Boxplots of the logistic regression combining ηVoigt and μVoigt for the 50 Hz excitations (a) and 75 Hz excitations (b), and of the μVoigt parameter alone for the 50 Hz excitations (c) and 75 Hz excitations (d)

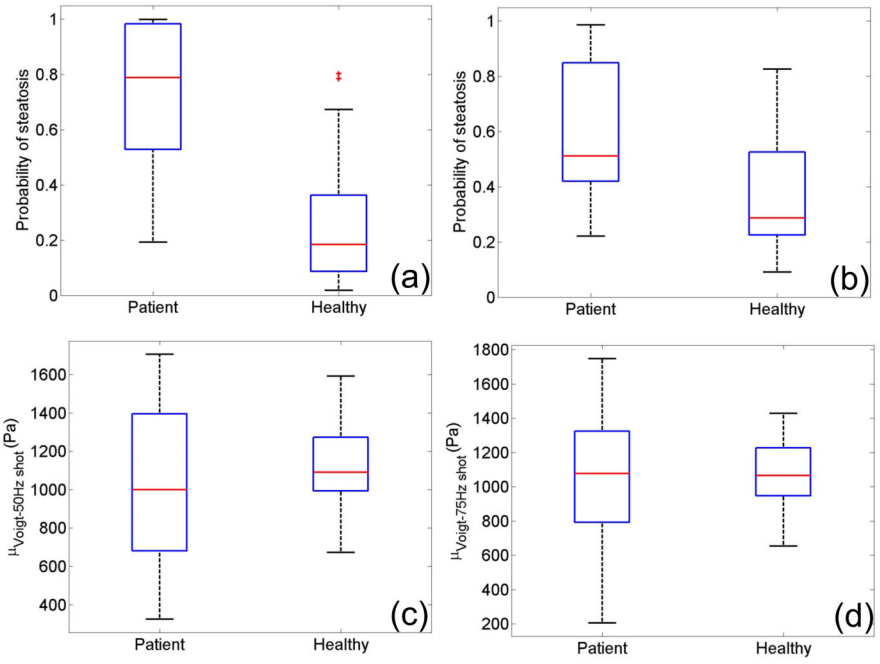

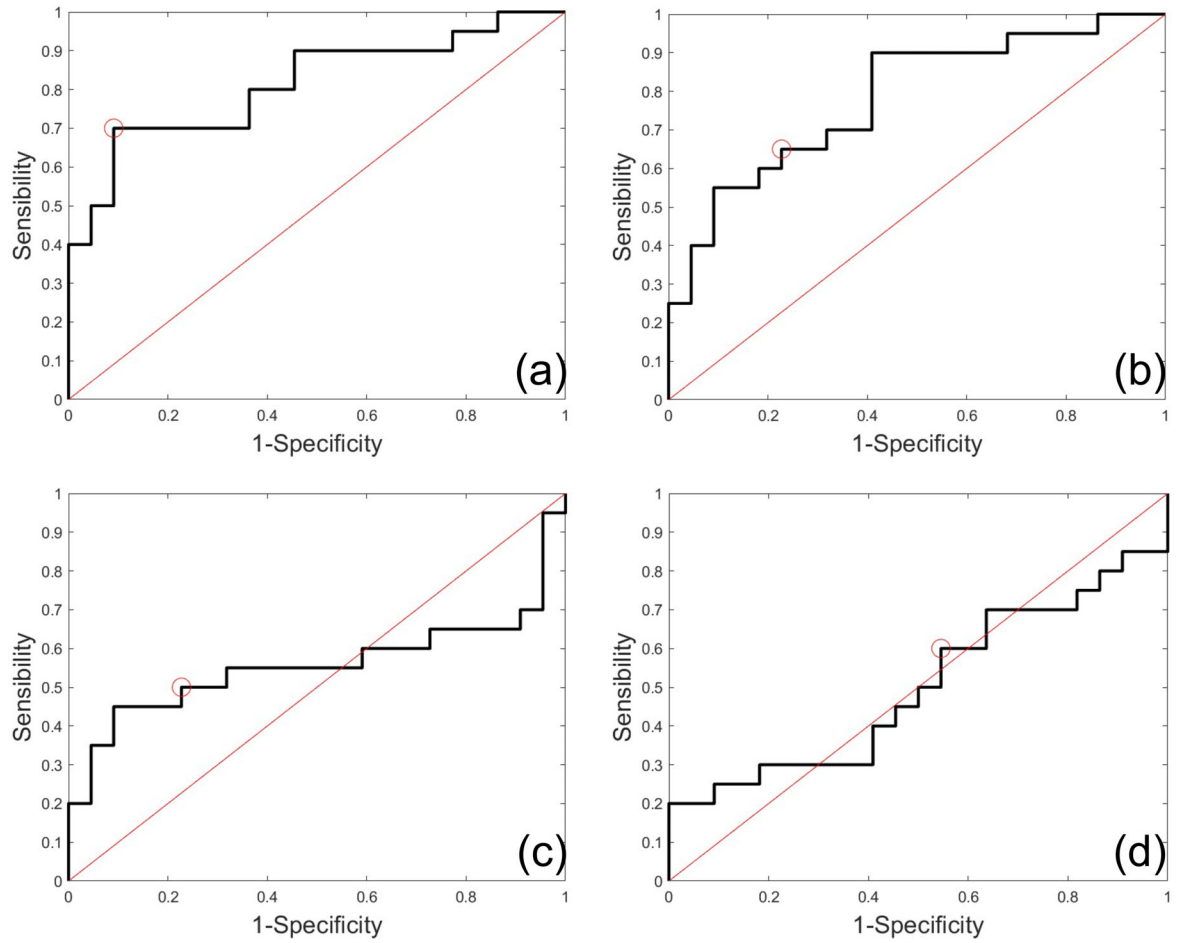

FIGURE 6 Receiving operator curve (ROC) curves for the diagnosis of steatosis of the parameters ηVoigt for both the 50 Hz excitations (a) and 75 Hz excitations (b) and μVoigt for both the 50 Hz excitations (c) and 75 Hz excitations (d). Red circles: optimal operating points

TABLE 2 Comparison of Fibroscan parameters for the diagnosis of steatosis. Values are expressed as median and quartiles. AUROC: area under the receiving operator curve; CI, confidence interval; (IQR), interquartile range

Parameter	Patients (median value/IQR)	Healthy volunteers (median value/IQR)	*p*-value	AUROC (95% CI)	Sensitivity (95% CI)	Specificity (95% CI)
ηVoigt (50 Hz) (Pa.s)	3.0	2.1	<0.001	0.814	70.0	90.9
	(2.3–3.3)	(1.7–2.4)		(0.680–0.947)	(49.9–90.1)	(78.9–100.0)
ηVoigt (75 Hz) (Pa.s)	2.3	1.8	0.002	0.784	65.0	77.3
	(1.9–2.8)	(1.7–2.1)		(0.642–0.926)	(44.1–85.9)	(59.8–94.8)
μVoigt (50 Hz) (Pa)	999	1091	0.537	0.557	50.0	77.3
	(681–1396)	(992–1274)		(0.381–0.733)	(28.1–71.9)	(59.8–94.8)
μVoigt (75 Hz) (Pa)	1077	1064	1	0.500	60.0	45.5
	(793–1325)	(947–1226)		(0.323–0.677)	(38.5–81.5)	(24.6–66.3)
μFibroscan (50 Hz) (Pa)	2575	1417	<0.001	0.891	80.0	95.5
	(2000–3117)	(1183–1667)		(0.787–0.995)	(62.5–97.5)	(86.8–100.0)

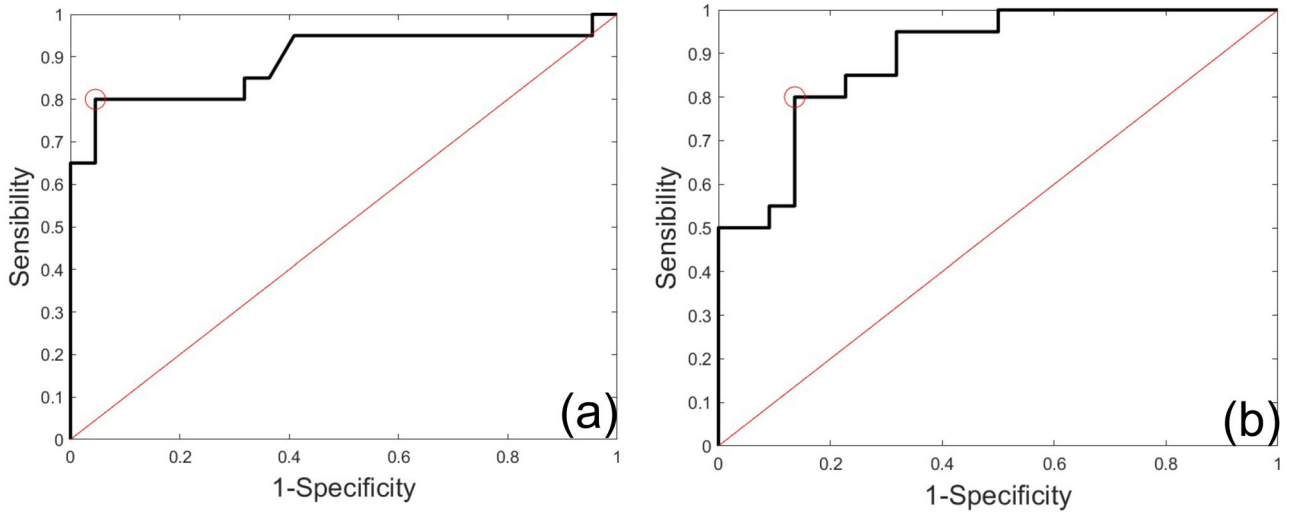

FIGURE 7 Receiving operator curve (ROC) curves for the diagnosis of steatosis of the parameters μFibroscan (a) and the logistic regression combining μVoigt and ηVoigt for the 50 Hz excitations (b). Red circles: optimal operating points

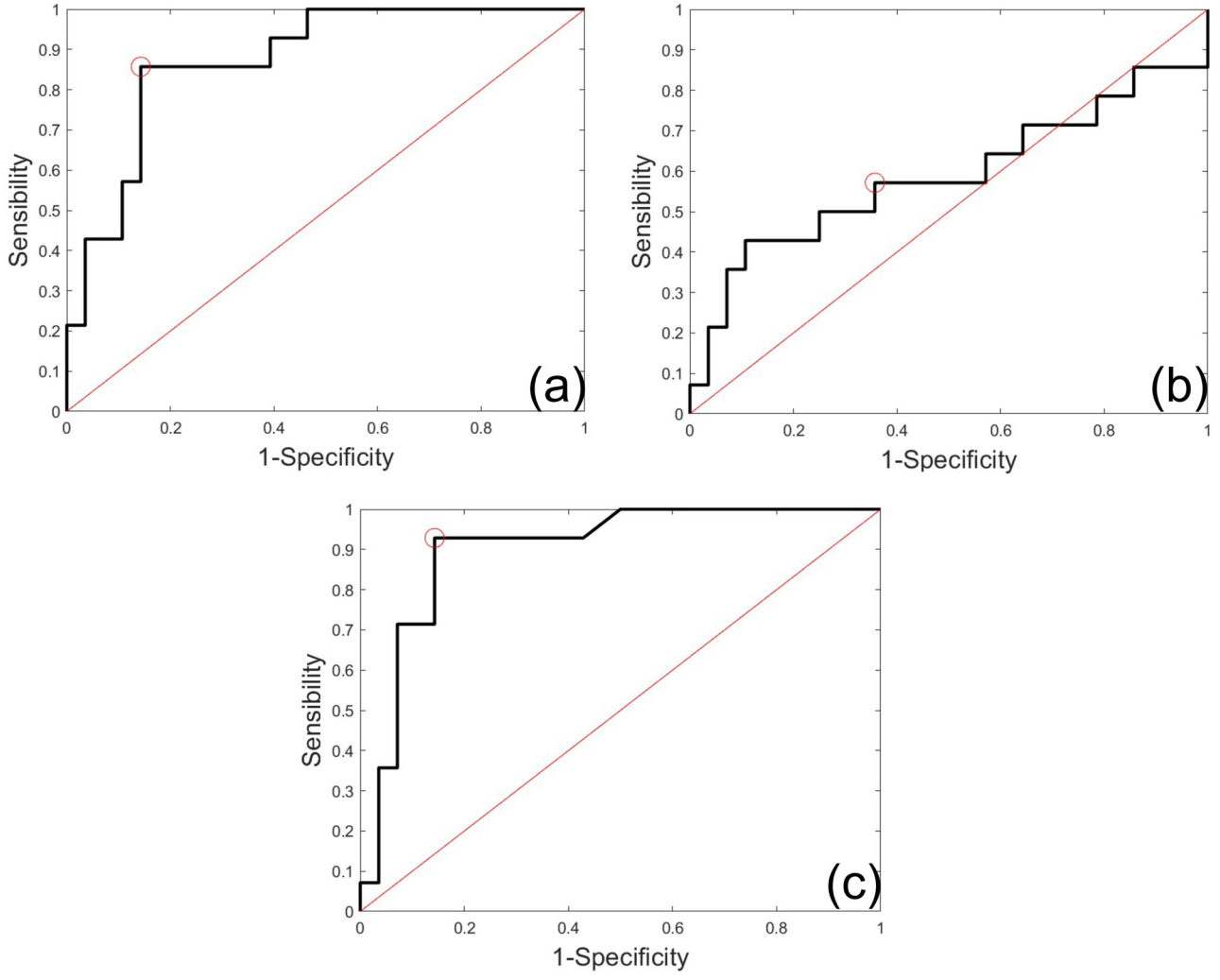

FIGURE 8 Receiving operator curve (ROC) curves comparing steatosis $\leq$ S1 versus $\geq$ S2 for the parameters ηVoigt (a), μVoigt (b) with the 50 Hz excitations, and μFibroscan (c). Red circles: optimal operating points

TABLE 3 Correlations between each of the different parameters

	ηVoigt (75 Hz)	μVoigt (50 Hz)	μVoigt (75 Hz)	μFibroScan (50 Hz)	μFibroScan (75 Hz)
ηVoigt (50 Hz)	$r = 0.86$	$r = 0.33$	$r = 0.17$	$r = 0.75$	$r = 0.79$
	$p < 0.001$	$p = 0.03$	$p = 0.27$	$p < 0.001$	$p < 0.001$
ηVoigt (75 Hz)		$r = 0.27$	$r = 0.13$	$r = 0.62$	$r = 0.65$
		$p = 0.08$	$p = 0.43$	$p < 0.001$	$p < 0.001$
μVoigt (50 Hz)			$r = 0.78$	$r = 0.03$	$r = 0.09$
			$p < 0.001$	$p = 0.868$	$p = 0.58$
μVoigt (75 Hz)				$r = 0.07$	$r = 0.1$
				$p = 0.68$	$p = 0.53$
μFibroScan (50 Hz)					$r = 0.94$
					$p < 0.001$

4.6 | Impact of age on the measured parameters

There was no significant difference for all measured parameters between the two groups (p value ranging from 0.42 to 1).

5 | DISCUSSION

In this in vivo study, we have successfully applied a spectroscopy method associated with a Voigt rheological model on data acquired with a modified Fibroscan, enabling us to estimate the two components of the complex shear modulus of the liver: its shear viscosity and its shear elasticity. Among the parameters evaluated in our study, ηVoigt and μFibroscan where good indicators of the modifications of the viscous component of the liver induced by steatosis, and μVoigt was not. These findings were coherent with the Voigt model, and our expectations.

When comparing patients with healthy volunteers, we found that μFibroscan was significantly higher in patients than in volunteers, with a good diagnostic performance for steatosis diagnosis (AUROC = 0.891), this indicated that either viscosity or elasticity or both were increased in the patients' livers. When discriminating the viscoelastic components, we found that ηVoigt was significantly higher in patients with steatosis, whereas there were no significant differences for μVoigt between the two groups. To confirm these results, we found that ηVoigt presented a good diagnostic performance for steatosis comparing healthy volunteers versus patients with steatosis (AUROC = 0.814 and 0.784 for the 50 Hz excitations and 75 Hz excitations, respectively) and an even better one comparing grouped S0/S1 patients versus $\geq$ S2 (AUROC = 0.875 for the 50 Hz excitations). These results show that livers of patients with steatosis without or with low-grade fibrosis presented only an increased viscous component compared with livers of healthy volunteers, with no modification of the elastic component.

The originality of our method is the separated extraction of the elastic and the viscous components of the liver, that is, extracting μVoigt and ηVoigt from a Fibroscan acquisition by fitting the Voigt model to phase velocity data. In this context, it was necessary to observe whether the combination of these two parameters was correlated with μFibroscan obtained from the group shear wave speed at 50 Hz and compare the results concerning the differences between the two groups of patients. After realizing two logistic regressions, which allowed us to compare the combination of μVoigt and ηVoigt versus μFibroscan, we found a good correlation ($r = 0.78$) between the two criteria and also similar AUROC (0.893 and 0.891, respectively) for discriminating both groups. This strongly suggests that the two extracted parameters μVoigt and ηVoigt could be well correlated to liver stiffness and viscosity, respectively.

One of the reasons we used the Voigt model was its ease of use and its dispersion curve adjusted by the ratio $\eta\omega/\mu$ at low frequency, which was of interest in this setup. However, the comparison between experimental data and the Voigt model is not perfect. Future work could be conducted in this direction to use another rheological model, for example the Biot model, which considers the presence of fluid (blood) in the liver.[40] For measurements, other methods to estimate the phase velocity $c_s(f)$ evolution from the unwrap phase at each frequency could also be done. This would require taking all the data and analyzing it differently.

In the study by Nightingale et al.,[32] the Voigt model was not taken into account due to its complexity with upward and downward curvature of $c_s(f)$ with frequency. Nevertheless, for a low viscous effect compared to the shear elastic modulus ($\frac{\eta\omega}{\mu} \ll 1$), the shear velocity $c_s(f)$ evolution is quadratic with frequency and is easy to fit using a nonlinear minimization method even in noisy

measurements. Nightingale et al.[32] used a linear model $c_s(f) = c_0 + \frac{dc_s}{df} f$ where c_0 is the intercept at zero frequency, and $\frac{dc_s}{df}$ is the dispersion slope. Measurements at 200 Hz obtained from the dispersion curve $c_s(f)$ are also recorded in their work for comparison with the group velocity measurements obtained using Acoustic Radiation Force Imaging (ARFI)/Shear Wave Elastography Imaging. Nightingale et al. found no correlation between steatosis and any of the material model parameters, as evidenced by the AUROC values near 0.5 for each parameter. Their method required the use of an assumed material model, that is, the linear dispersion model in her case, and thus, conclusions drawn are subject to the validity of the assumptions in the model. In the work of Nightingale et al., the linear slope recorded from the patients is not compensated by shear elasticity magnitude as is the case with the Voigt model. In our work, a low $c_s(f)$ dispersion evolution, which is driven by $\frac{3}{8}(\frac{\omega\eta}{\mu})^2$, is not necessarily related to low viscosity η, but to a low ratio of viscosity to elasticity. This can result in fairly high viscosity values if, for instance, the shear elastic modulus μ is very high, which would result in a low viscosity to elasticity ratio. Thus, a small dispersion curve $\frac{dc_s}{df}$ in Nightingale et al.'s findings can correspond to a high viscosity with our inverse problem. Inversely, in Nightingale et al.'s Figure 6, where the dispersion curve $\frac{dc_s}{df}$ is plotted as a function of c_s(200 Hz), two different measurements situated at the same c_s(200 Hz) but with different slopes will be quantified as different in Nightingale et al.'s study but may give the same shear viscosity η_{Voigt} with our analysis. In this particular case, the two $c_s(f)$ curves cross each other at c_s(200 Hz) at 200 Hz, but the higher slope curve would, for example, give a small value of $\mu_{\text{Voigt}}^{\text{Small}}$ estimated at zero frequency, and a high $\frac{\eta_{\text{Voigt}}\omega}{\mu_{\text{Voigt}}^{\text{Small}}}$ ratio. Alternatively, the lower slope curve would give a high value of $\mu_{\text{Voigt}}^{\text{High}}$ estimated at zero frequency and then a low $\frac{\eta_{\text{Voigt}}\omega}{\mu_{\text{Voigt}}^{\text{High}}}$ ratio. Thus, two different dispersion slopes can give the same shear viscosity η_{Voigt}. For these reasons, the results obtained from these two different spectroscopy analyses are difficult to compare.

Nevertheless, as mentioned above, we found that μFibroscan extracted from the standard group velocity method was significantly higher in patients than in volunteers, with a good diagnostic performance for steatosis diagnosis (AUROC = 0.891). This result is not consistent with some of the literature using ARFI.[32,41] For example, in the study of Nightingale et al.,[32] the group velocity obtained by ARFI has an AUROC value of 0.49 for separation of steatosis grade $\leq$ S1 and $\geq$ S2. However, other results published in 2017 show the same trend as ours. Guo et al.[42] evaluated the utility of ARFI in determining the severity grade of steatosis in rat livers and to investigate the changes in various histologic and biochemical characteristics. Steatosis was induced in the livers of 57 rats by gavage feeding of a high fat emulsion; 12 rats received a standard diet and served as controls. They found a higher shear wave velocity (SWV), measured with the ARFI method, in the fatty liver group than in the control group (respectively SWV = 2.83 $\pm$ 0.37 m/s vs. 2.25 $\pm$ 0.52 m/s). SWV measurements had a high accuracy in predicting steatosis grade ($\geq$ S1), with an AUROC of 0.82, and the optimal cutoff value was 2.59 with a sensitivity of 88% and specificity of 76%. Moreover, recent clinical studies showed that steatosis could induce an overestimation of fibrosis with the Fibroscan measures,[43,44] although this remains open to debate.[45]

We found that μFibroscan was moderately correlated with MRI fat fraction ($r = 0.54$), and when separating the liver viscoelastic components, we found a similar moderate correlation between ηVoigt and MRI fat fraction ($r = 0.49$) and an absence of correlation between μVoigt and MRI fat fraction ($r = 0.16$). These moderate correlations could be due to the inherent inhomogeneity of steatosis in the liver: our VCTE spectroscopy measurements and the liver biopsies were performed in similar areas of the liver, whereas the MRI fat fraction ROIs were placed in three different parts of the liver. Nevertheless, we have shown that shear viscosity ηVoigt was positively correlated with the stage of steatosis. This may suggest that the sensitivity of the ηVoigt parameter to steatosis may be based on physical reasons other than the percentage of fat. Furthermore, the analysis of the influence of the liver blood perfusion on the viscoelastic parameters obtained by shear wave spectroscopy and the quantification of the possible relation between steatosis grade obtained by MRI and liver blood perfusion may be of further interest. Recent ultrasensitive US Doppler methods open these possibilities with[46] or without[47] the use of US contrast agents.

Unfortunately, we could not directly compare our method with CAP because it was not available to us when we conducted the study, and our FibroScan data cannot be used to calculate CAP retrospectively. However, ηVoigt for the 50 Hz excitations presents an AUROC of 0.814 (0.680–0.947) for the diagnosis of steatosis S0 versus $\geq$S1, which is a similar value to what Karlas et al. found for CAP in their recent meta-analysis (AUROC of 0.823 for steatosis S0 versus $\geq$S1).[48]

Several limitations are worth mentioning. Firstly, we had a relatively small study sample due to our restrictive exclusion criteria and our single center recruitment. Recruitment within a year of patients with steatosis confirmed by liver biopsy but without a severe fibrosis (fibrosis > F2 using SAF score) was limited. A second limitation was the difficulty in obtaining valid measurements on a number of obese patients with the Fibroscan M probe, furthermore, a dedicated study evaluating the performance of ηVoigt measurements with the Fibroscan XL probe would be useful. Finally, we did not assess the reproducibility of the acquisition and the

postprocessing. We did however use the median of multiple measurements (we excluded those not validated by the standard Fibroscan algorithm) in order to have more reliable values, thus limiting intraobserver variability.

6 | CONCLUSION

We present a promising novel method of assessing liver steatosis using shear wave spectroscopy and dispersion analysis with the FibroScan. The diagnostic performance of the method seems comparable to CAP, and its major advantage is the separate evaluation of liver shear elasticity and shear viscosity, this evaluation could in turn decrease the rate of false positives of fibrosis with the FibroScan in patients suffering from steatosis. However, additional studies to evaluate the technique are warranted, notably in terms of reproducibility, the possibility of steatosis grading, and measurements of elasticity with the Voigt model for fibrosis evaluation.

Finally, as mentioned in the discussion, the analysis of liver blood perfusion conjointly with the liver viscoelastic moduli could provide additional information that would explain the increased shear viscosity during steatosis.

ACKNOWLEDGMENTS

This work has been funded in part by The Regional University Hospital of Tours, Echosens, Paris, and The University of Tours.

CONFLICT OF INTEREST

The authors have no conflict of interest to disclose.

DATA AVAILABILITY STATEMENT

Data are available on request from the authors.

REFERENCES

1. Mantovani A, Scorletti E, Mosca A, Alisi A, Byrne CD, Targher G. Complications, morbidity and mortality of nonalcoholic fatty liver disease. *Metabolism*. 2020;111S:154170. https://doi.org/10.1016/j.metabol.2020.154170
2. Younossi ZM, Koenig AB, Abdelatif D, Fazel Y, Henry L, Wymer M. Global epidemiology of nonalcoholic fatty liver disease-Meta-analytic assessment of prevalence, incidence, and outcomes. *Hepatol Baltim Md*. 2016;64(1):73-84. https://doi.org/10.1002/hep.28431
3. Bellentani S, Scaglioni F, Marino M, Bedogni G. Epidemiology of non-alcoholic fatty liver disease. *Dig Dis*. 2010;28(1):155-161. https://doi.org/10.1159/000282080
4. Blachier M, Leleu H, Peck-Radosavljevic M, Valla DC, Roudot-Thoraval F. The burden of liver disease in Europe: a review of available epidemiological data. *J Hepatol*. 2013;58(3):593-608. https://doi.org/10.1016/j.jhep.2012.12.005
5. Chalasani N, Younossi Z, Lavine JE et al. The diagnosis and management of nonalcoholic fatty liver disease: practice guidance from the American Association for the Study of Liver Diseases. *Hepatology*. 2018;67(1):328-357. https://doi.org/10.1002/cld.722
6. Byrne CD, Targher G. NAFLD: a multisystem disease. *J Hepatol*. 2015;62(1): S47-S64. https://doi.org/10.1016/j.jhep.2014.12.012
7. Musso G, Gambino R, Tabibian JH, et al. Association of non-alcoholic fatty liver disease with chronic kidney disease: a systematic review and meta-analysis. *PLoS Med*. 2014;11(7):e1001680. https://doi.org/10.1371/journal.pmed.1001680
8. Brunt EM, Janney CG, Di Bisceglie AM, Neuschwander-Tetri BA, Bacon BR. Nonalcoholic steatohepatitis: a proposal for grading and staging the histological lesions. *Am J Gastroenterol*. 1999;94(9):2467-2474. https://doi.org/10.1111/j.1572-0241.1999.01377.x
9. Kleiner DE, Brunt EM, Van Natta M, et al. Design and validation of a histological scoring system for nonalcoholic fatty liver disease. *Hepatol Baltim Md*. 2005;41(6):1313-1321. https://doi.org/10.1002/hep.20701
10. Bravo AA, Sheth SG, Chopra S. Liver biopsy. *N Engl J Med*. 2001;344(7):495-500. https://doi.org/10.1056/NEJM200102153440706
11. Karanjia RN, Crossey MME, Cox IJ, et al. Hepatic steatosis and fibrosis: non-invasive assessment. *World J Gastroenterol*. 2016;22(45):9880-9897. https://doi.org/10.3748/wjg.v22.i45.9880
12. European Association for the Study of the Liver (EASL), European Association for the Study of Diabetes (EASD), European Association for the Study of Obesity (EASO). EASL-EASD-EASO Clinical Practice Guidelines for the management of non-alcoholic fatty liver disease. *J Hepatol*. 2016;64(6):1388-1402. https://doi.org/10.1016/j.jhep.2015.11.004
13. Bohte AE, van Werven JR, Bipat S, Stoker J. The diagnostic accuracy of US, CT, MRI and 1H-MRS for the evaluation of hepatic steatosis compared with liver biopsy: a meta-analysis. *Eur Radiol*. 2011;21(1):87-97. https://doi.org/10.1007/s00330-010-1905-5
14. Hamer OW, Aguirre DA, Casola G, Lavine JE, Woenckhaus M, Sirlin CB. Fatty liver: imaging patterns and pitfalls. *RadioGraphics*. 2006;26(6):1637-1653. https://doi.org/10.1148/rg.266065004
15. Stern C, Castera L. Non-invasive diagnosis of hepatic steatosis. *Hepatol Int*. 2017;11(1):70-78. https://doi.org/10.1007/s12072-016-9772-z
16. Szczepaniak LS, Nurenberg P, Leonard D, et al. Magnetic resonance spectroscopy to measure hepatic triglyceride content: prevalence of hepatic steatosis in the general population. *Am J Physiol Endocrinol Metab*. 2005;288(2):E462-E468. https://doi.org/10.1152/ajpendo.00064.2004
17. Caussy C, Reeder SB, Sirlin CB, Loomba R. Noninvasive quantitative assessment of liver fat by MRI-PDFF as an endpoint in NASH trials. *Hepatology*. 2018;68(2):763-772. https://doi.org/10.1002/hep.29797
18. Purcell Y, Copin P, Paradis V, Vilgrain V, Ronot M. Lessons learnt from pathologic imaging correlation in the liver: an historical perspective. *Br J Radiol*. 2019;92(1097):20180701. https://doi.org/10.1259/bjr.20180701. Published online January 10, 2019:20180701.
19. Byrne CD, Targher G. Time to replace assessment of liver histology with MR-based imaging tests to assess efficacy of interventions for nonalcoholic fatty liver disease. *Gastroenterology*. 2016;150(1):7-10. https://doi.org/10.1053/j.gastro.2015.11.016
20. Imbault M. Quantitative and functional ultrafast ultrasound imaging of the human brain. May 3, 2017. Accessed December 2, 2019. http://www.theses.fr/2017USPCC158
21. Imbault M, Faccinetto A, Osmanski BF, et al. Robust sound speed estimation for ultrasound-based hepatic steatosis assessment. *Phys Med Biol*. 2017;62(9):3582-3598. https://doi.org/10.1088/1361-6560/aa6226
22. de Lédinghen V, Wong GLH, Vergniol J, et al. Controlled attenuation parameter for the diagnosis of steatosis in non-alcoholic fatty liver disease. *J Gastroenterol Hepatol*. 2016;31(4):848-855. https://doi.org/10.1111/jgh.13219
23. Mikolasevic I, Orlic L, Franjic N, Hauser G, Stimac D, Milic S. Transient elastography (FibroScan®) with controlled attenuation parameter in the assessment of liver steatosis and

fibrosis in patients with nonalcoholic fatty liver disease - where do we stand?. *World J Gastroenterol*. 2016;22(32):7236-7251. https://doi.org/10.3748/wjg.v22.i32.7236
24. Sasso M, Tengher-Barna I, Ziol M, et al. Novel controlled attenuation parameter for noninvasive assessment of steatosis using Fibroscan®: validation in chronic hepatitis C. *J Viral Hepat*. 2012;19(4):244-253. https://doi.org/10.1111/j.1365-2893.2011.01534.x
25. Xu L, Lu W, Li P, Shen F, Mi YQ, Fan JG. A comparison of hepatic steatosis index, controlled attenuation parameter and ultrasound as noninvasive diagnostic tools for steatosis in chronic hepatitis B. *Dig Liver Dis*. 2017;49(8):910-917. https://doi.org/10.1016/j.dld.2017.03.013
26. Yen YH, Chen JF, Wu CK, et al. The correlation of controlled attenuation parameter results with ultrasound-identified steatosis in real-world clinical practice. *J Formos Med Assoc*. 2017;116(11):852-861. https://doi.org/10.1016/j.jfma.2017.08.010
27. Sandrin L, Fourquet B, Hasquenoph JM, et al. Transient elastography: a new noninvasive method for assessment of hepatic fibrosis. *Ultrasound Med Biol*. 2003;29(12):1705-1713. https://doi.org/10.1016/j.ultrasmedbio.2003.07.001
28. Lédinghen Vde, Bail BL, Rebouissoux L, et al. Liver stiffness measurement in children using fibroscan: feasibility study and comparison with fibrotest, aspartate transaminase to platelets ratio index, and liver biopsy. *J Pediatr Gastroenterol Nutr*. 2007;45(4):443-450. https://doi.org/10.1097/MPG.0b013e31812e56ff
29. Ferraioli G. Review of liver elastography guidelines. *J Ultrasound Med Off J Am Inst Ultrasound Med*. 2019;38(1):9-14. https://doi.org/10.1002/jum.14856
30. Liu Z, Bilston L. On the viscoelastic character of liver tissue: experiments and modelling of the linear behaviour. *Biorheology*. 2000;37(3):191-201.
31. Muller M, Gennisson JL, Deffieux T, Tanter M, Fink M. Quantitative viscoelasticity mapping of human liver using supersonic shear imaging: preliminary in vivo feasibility study. *Ultrasound Med Biol*. 2009;35(2):219-229. https://doi.org/10.1016/j.ultrasmedbio.2008.08.018
32. Nightingale KR, Rouze NC, Rosenzweig SJ, et al. Derivation and analysis of viscoelastic properties in human liver: impact of frequency on fibrosis and steatosis staging. *IEEE Trans Ultrason Ferroelectr Freq Control*. 2015;62(1):165-175. https://doi.org/10.1109/TUFFC.2014.006653
33. Sandrin L, Cassereau D, Fink M. The role of the coupling term in transient elastography. *J Acoust Soc Am*. 2003;115(1):73-83. https://doi.org/10.1121/1.1635412
34. Aki K, Richards P. *Quantitative Seismology*. University Science Books; 2002.
35. Deffieux T, Montaldo G, Tanter M, Fink M. Shear wave spectroscopy for in vivo quantification of human soft tissues viscoelasticity. *IEEE Trans Med Imaging*. 2009;28(3):313-322. https://doi.org/10.1109/TMI.2008.925077
36. Leclerc GE, Charleux F, Robert L, et al. Analysis of liver viscosity behavior as a function of multifrequency magnetic resonance elastography (MMRE) postprocessing. *J Magn Reson Imaging*. 2013;38(2):422-428. https://doi.org/10.1002/jmri.23986
37. Catheline S, Gennisson JL, Delon G, et al. Measuring of viscoelastic properties of homogeneous soft solid using transient elastography: an inverse problem approach. *J Acoust Soc Am*. 2004;116(6):3734-3741.
38. Bedossa P, FLIP Pathology Consortium. Utility and appropriateness of the fatty liver inhibition of progression (FLIP) algorithm and steatosis, activity, and fibrosis (SAF) score in the evaluation of biopsies of nonalcoholic fatty liver disease. *Hepatol Baltim Md*. 2014;60(2):565-575. https://doi.org/10.1002/hep.27173
39. Bedossa P, Poitou C, Veyrie N, et al. Histopathological algorithm and scoring system for evaluation of liver lesions in morbidly obese patients. *Hepatol Baltim Md*. 2012;56(5):1751-1759. https://doi.org/10.1002/hep.25889
40. Catheline S, Aichele J. Fluids alter elasticity measurements: porous wave propagation accounts for shear wave dispersion in elastography. *Front Phys*. 2021. https://doi.org/10.3389/fphy.2021.697990
41. Palmeri ML, Wang MH, Rouze NC, et al. Noninvasive evaluation of hepatic fibrosis using acoustic radiation force-based shear stiffness in patients with nonalcoholic fatty liver disease. *J Hepatol*. 2011;55(3):666-672. https://doi.org/10.1016/j.jhep.2010.12.019
42. Guo Y, Dong C, Lin H, et al. Ex vivo study of acoustic radiation force impulse imaging elastography for evaluation of rat liver with steatosis. *Ultrasonics*. 2017;74:161-166. https://doi.org/10.1016/j.ultras.2016.10.009
43. Petta S, Wong VWS, Cammà C, et al. Improved noninvasive prediction of liver fibrosis by liver stiffness measurement in patients with nonalcoholic fatty liver disease accounting for controlled attenuation parameter values. *Hepatology*. 2017;65(4):1145-1155. https://doi.org/10.1002/hep.28843
44. Petta S, Maida M, Macaluso FS, et al. The severity of steatosis influences liver stiffness measurement in patients with nonalcoholic fatty liver disease. *Hepatology*. 2015;62(4):1101-1110. https://doi.org/10.1002/hep.27844
45. Eddowes PJ, Sasso M, Allison M, et al. Accuracy of FibroScan controlled attenuation parameter and liver stiffness measurement in assessing steatosis and fibrosis in patients with nonalcoholic fatty liver disease. *Gastroenterology*. 2019;156(6):1717-1730. https://doi.org/10.1053/j.gastro.2019.01.042
46. Errico C, Pierre J, Pezet S, et al. Ultrafast ultrasound localization microscopy for deep super-resolution vascular imaging. *Nature*. 2015;527(7579):499-502. https://doi.org/10.1038/nature16066
47. Baranger J, Arnal B, Perren F, Baud O, Tanter M, Demene C. Adaptive spatiotemporal SVD clutter filtering for ultrafast doppler imaging using similarity of spatial singular vectors. *IEEE Trans Med Imaging*. 2018;37(7):1574-1586. https://doi.org/10.1109/TMI.2018.2789499
48. Karlas T, Petroff D, Sasso M, et al. Individual patient data meta-analysis of controlled attenuation parameter (CAP) technology for assessing steatosis. *J Hepatol*. 2017;66(5):1022-1030. https://doi.org/10.1016/j.jhep.2016.12.022

SUPPORTING INFORMATION

Additional supporting information may be found in the online version of the article at the publisher's website.

How to cite this article: Pearson A, Dujardin P-A, d'Alteroche L, et al. Vibration-controlled transient elastography for noninvasive evaluation of liver steatosis. *Med Phys*. 2022;49:1507–1521. https://doi.org/10.1002/mp.15484